Research Article

Influence of Re and Ru doping on the structural, optical and photocatalytic properties of nanocrystalline TiO_2

Beatriz Barrocas[1] · Olinda C. Monteiro[1] · Manuel R. Nunes[1] · António J. Silvestre[2,3,4]

Abstract

TiO_2 and TM-doped TiO_2 (TM = Re, Ru) anatase crystalline nanopowders were synthesized by a simple hydrothermal method. Samples with nominal TM/Ti ratio of 0.01 were prepared for this study. Their structural, microstructural and optical properties were studied. The lattice parameters of the different prepared samples were calculated and their mean crystallite sizes determined to be in the range 15–7 nm, the lower values being obtained for the doped crystallites. The samples' specific surface areas were determined and correlated with their mean crystallite sizes. The incorporation of the dopant elements results in an increase of the optical absorption in the visible range. The samples' optical bandgap and Urbach energies were calculated from UV–Vis diffuse reflectance spectra. The photocatalytic behavior of the synthesized samples was investigated for the rhodamine B and phenol degradation processes, the kinetics of the different photo-oxidation reactions being also studied. The results showed that doping either with Re or Ru can lead to enhancement of the TiO_2 photocatalytic efficiency and that, among the synthesized samples Ru-doped TiO_2 is the most efficient photocatalyst for both the Rhodamine B and phenol photodegradation reactions.

Keywords TM-TiO_2 nanoparticles · Optical bandgap · Urbach energy · Photocatalysis · Organic pollutants

1 Introduction

Organic pollutants with high toxicity and difficult degradation features have been a growing concern due to their detrimental environmental and ecological impact. Thus, the development of efficient processes to remove recalcitrant organic substances from wastewaters and air has been attracting a great attention and is currently a research topic of major importance. Different oxidation processes are currently used to oxidise organic compounds and convert them into less harmful end products or even lead to their complete mineralization into CO_2 and H_2O [1–5]. Among them, semiconductor heterogeneous photocatalysis has enormous potential to treat organic contaminants, having gained growing acceptance as an effective wastewater treatment method to degrade a broad variety of harmful compounds. Although a wide variety of semiconductors have been reported to be effective photocatalysts [4–13], TiO_2 is still the most widely used semiconductor in photocatalysis because it is a cost effective non-toxic compound, chemically and biologically inert, thermally stable, superhydrophilic, and capable of promoting the oxidation of numerous organic compounds [14–20].

TiO_2 is a wide bandgap metal oxide semiconductor that can occur at standard temperature and pressure in three polymorphic phases: *rutile*, *anatase* and *brookite*. Among them, *rutile* and *anatase* phases are those that present the greatest technological interest. The *rutile* phase has an indirect bandgap of ~ 3 eV and exhibits a tetragonal

✉ Olinda C. Monteiro, ocmonteiro@fc.ul.pt; ✉ António J. Silvestre, asilvestre@adf.isel.pt | [1]CQB/CQE, Faculdade de Ciências, Universidade de Lisboa, Lisboa, Portugal. [2]Departamento de Física, Instituto Politécnico de Lisboa, ISEL – Instituto Superior de Engenharia de Lisboa, Lisboa, Portugal. [3]LSPL and CeFEMA, Departamento de Física, Faculdade de Ciências, Universidade de Lisboa, Lisboa, Portugal. [4]Departamento de Física, Instituto Superior Técnico, Universidade de Lisboa, Lisboa, Portugal.

SN Applied Sciences (2019) 1:556 | https://doi.org/10.1007/s42452-019-0567-4

Received: 12 March 2019 / Accepted: 6 May 2019 / Published online: 13 May 2019

structure with a P42/*mnm* space group and standard lattice parameters $a = b = 4.584$ Å and $c = 2.953$ Å [21]. The *anatase* phase has an indirect bandgap of ~ 3.2 eV, exhibiting also a tetragonal structure with a I41/*amd* space group and standard lattice parameters $a = b = 3.7852$ Å and $c = 9.5139$ Å [22]. Both phases consist of different arrangements of the same TiO_6 building block, where the Ti atom sits at the center and is surrounded by six O atoms at the corners of a distorted octahedron. *Rutile* is the most closed structure, being almost 10% denser than *anatase*. *Rutile* is thermodynamically stable at any temperature while *anatase* phase is metastable at temperatures below 600 °C [23], although in the form of nanoparticles it can be stable up to 800 °C [24]. In particular, TiO_2-*anatase* exhibits the highest photocatalytic activity [17, 25–27].

The TiO_2 photocatalytic ability to degrade organic pollutants in aqueous solutions results from the photogenerated electron–hole pairs promoted upon the absorption of UV light, and their ability to inducing the formation hydroxyl radicals [28–32]. These radicals are strong oxidizing species that interacts with the organic pollutants present in the aqueous solution, leading to their progressive degradation and subsequently mineralization [30–32]. However, the application of TiO_2 as photocatalyst is yet limited by the high recombination rate of photocharge carriers and its wide bandgap, which lie in the UV region. Therefore, much effort has been expended to reduce the recombination rate of TiO_2 and to enhance its photocatalytic efficiency under both UV and visible light irradiation. Several approaches have been undertaken, including doping with non-metals such N, C and S [33–36], transition metals (TM) including Fe, Co, Cr, Cu, Mo and Ta [37–43] or rare earth metals such as Ce, La, Eu and Ga [44–49], inducing structural defects such as Ti^{3+} or oxygen vacancies [50–52], and coupling TiO_2 with noble metals [14, 53, 54], narrow bandgap semiconductors [55, 56], hydroxyapatite [57] or graphene [54] giving rise to TiO_2-based hybrid structures with improved properties. Among the different approaches, the incorporation of dopants in low concentrations into the TiO_2 lattice have been shown to be a simple an effective way to reduce the electron–hole recombination rate and enhance absorption in the visible region of the electromagnetic spectrum. In particular, TM doping may induce structural defects and localized *d*-band states in the forbidden gap region that may decrease the bandgap energy and act also as active trap centers of electrons to reduce charge carrier recombination [41, 58–60]. In addition to structure and compositions leading to lower recombination rates and to more efficient radiation absorption, TiO_2-based photocatalysts should have high adsorption capability and thus a high specific surface area. However, it is still a challenge to prepare semiconductor nanocrystals with controllable size, shape and doping. In particular, the synthesis of nanoparticles with sizes under 10 nm still remains a major challenge. They usually require complex synthesis procedures and/or suffer from aggregation or poor monodispersity, which strongly compromise their photocatalytic efficiency and limit their large-scale industrial production.

This work reports on the synthesis of TiO_2, Re-doped TiO_2 and Ru-doped TiO_2 *anatase* nanoparticles by a swift and cost effective hydrothermal method and on their structural, microstructural and optical properties. The photocatalytic ability of the prepared samples for the degradation of organic pollutants under UV–Vis irradiation was evaluated using both rhodamine B (RhB) and phenol as pollutant models, the kinetics of the different photo-oxidation reactions being also studied.

2 Experimental

2.1 Materials

All reagents were of analytical grade and were used as received. Solutions were prepared with bi-distilled water.

2.2 Nanoparticles synthesis

The undoped TiO_2 and TM-doped TiO_2 samples were prepared as follows: a $TiCl_3$ solution (10 wt% in 20–30 wt% HCl) diluted in a ratio of 1:2 in 2 M HCl was used as the Ti source. To this solution a NH_4OH 4 M solution was added dropwise under vigorous stirring, until the complete precipitation of a white solid. The resulting suspension was kept at rest for 15 h at room temperature, and then filtered and rinsed with deionised water in order to remove the remaining ammonium and chloride ions. Crystallization of the TiO_2 precursor was done in aqueous solution in an autoclave at a temperature of 200 °C, for 6 h. Re-doped and Ru-doped TiO_2 nanopowders were synthesised using the same chemical procedure by adding the required molar amount of metal trichloride to the titanium trichloride solution. Samples with nominal TM/Ti atomic ratio of 0.01 were prepared for this comparative study. TiO_2 sample is white while $Ti_{0.99}Re_{0.01}O_2$ and $Ti_{0.99}Ru_{0.01}O_2$ samples are grey in colour.

2.3 Photodegradation experiments

The photodegradation experiments were conducted using a 250 mL refrigerated photo-reactor [11]. As a radiation source, it was used a 450 W Hanovia medium-pressure mercury-vapour lamp, the total irradiated energy being 40–48% in the ultraviolet range and 40–43% in the visible region.

Rhodamine B and phenol were used as pollutant models to evaluate the photocatalytic activity of the different prepared nanopowders under UV–vis irradiation. The catalytic photodegradation experiments were performed by adding 20 mg of powder to 150 mL of a 10 ppm RhB and 20 ppm phenol solutions. Three runs were performed for each photodegradation experiment (error < 6%). Prior to irradiation, suspensions were stirred in darkness for 60 min to ensure adsorption equilibrium. During irradiation, suspensions were sampled at regular intervals, centrifuged and analyzed by UV–vis or by gas chromatography–mass spectrometry (GC–MS), depending on the organic compound (see below). For convenience, the adsorption period is marked as – 60 min in the graphics.

2.4 Characterization

X-ray powder diffraction was done with a Philips X-ray diffractometer (PW 1730) with automatic data acquisition (APD Philips v3.6B), using Cu *Kα* radiation ($\lambda = 0.15406$ nm) and working at 40 kV/30 mA. The diffraction patterns were collected in the 2θ range of 20°–60° with a 0.02° step size and an acquisition time of 2.0 s/step. An instrumental broadening of 1.61×10^{-3} rad was measured from a standard macrocrystalline and strain-free silicon sample. The $K\alpha_2$ contribution was removed before the XRD data treatments. The 2θ angular position of the diffraction peaks and their full-width at half-maximum, β, were calculated by fitting the experimental diffraction lines with a Pseudo-Voigt function. The β values were corrected taking into account the instrumental broadening.

Transmission electron microscopy (TEM) images were taken with a JEOL 200CX electron microscope operating at 200 kV. Specific surface areas were obtained by the Brunauer–Emmett–Teller (B.E.T.) method, from nitrogen (Air Liquide, 99.999%) adsorption data at – 196 °C, using a Quantachrome mod NOVA 2200e volumetric apparatus. The samples, weighing approximately 55 mg, were previously degassed for 2.5 h at 300 °C at a pressure lower than 0.133 Pa. A SpexFlourolog 3–22/Tau 3 equipment was used for photoluminescence (PL) spectra measurements, with excitation and emission wavelength at 315 and 425 nm for TA solutions and using 280 mn excitation wavelength for solids analyses. The diffuse reflectance spectra (DRS) were obtained using a spectrometer Shimadzu UV-2600PC equipped with an ISR 2600plus integrating sphere. The same equipment was used for monitoring the absorption of the RhB solutions. The phenol solutions were monitored using a GC–MS, products conversion was monitored by taking samples and analysing them using a Shimadzu QP2100-Plus GC/MS system with a Tecknokroma TRB-5MS capillary column.

3 Results and discussion

3.1 Structure and morphology

Figure 1 shows the diffractograms of the undoped and TM-doped TiO_2 prepared samples. The diffraction reflections were indexed to the TiO_2 tetragonal *anatase* phase, using the ICDD-JCPDS Database Card No. 21-1272. All the XRD patterns show broad peaks matching the expected diffraction peaks of the (101), (103), (004), (112), (200), (105) and (211) *anatase* TiO_2 planes, with similar relative intensities to the standard database card. No traces of *rutile* or *brookite* secondary phases were observed. Furthermore, the XRD patterns of all doped samples show no signs of undesirable phases such as TM-dopant clusters or TM oxides. This result seems to support the assumption that the dopant elements are homogeneously distributed in the *anatase* matrix as intended. Taking into account Bragg's law $d_{hkl} = \lambda/2 \sin \theta_{hkl}$ and the 2θ angular positions of the (101) and (200) peaks in the XRD patterns of Fig. 1, the lattice parameters *a* and *c* as well as the unit

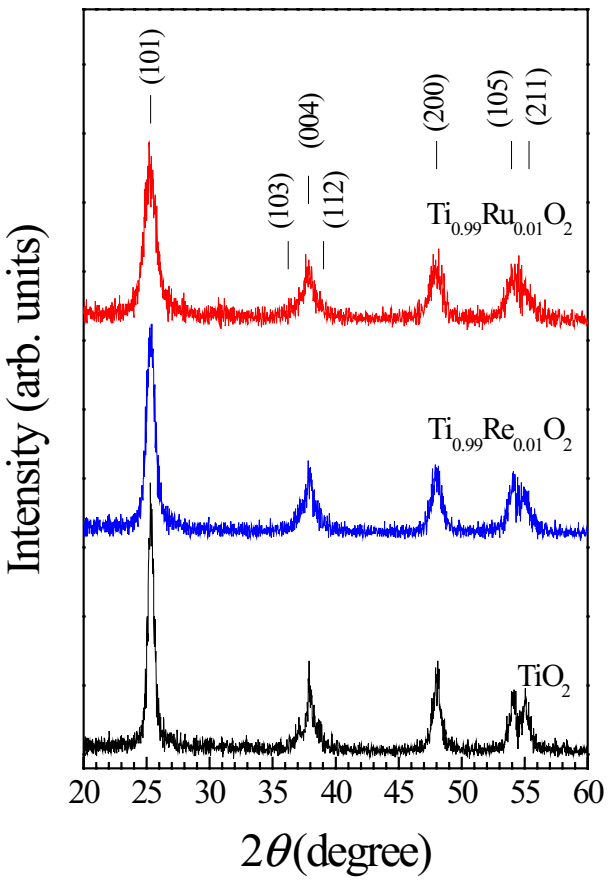

Fig. 1 X-ray diffraction patterns of the undoped TiO_2, Re-doped TiO_2 and Ru-doped TiO_2 nanoparticle samples

cell volumes, $V_{cell} = a^2c$, of the synthesized samples were calculated (see Table 1). The obtained lattice parameters for the undoped TiO_2 nanoparticles are in good agreement with the parameters reported in the standard TiO_2 *anatase* ICDD-JCPDS Database Card No. 21-1272, showing that the unit cell volume contracted only 1.2% relative to its standard value. On the other hand, the Re- and Ru-doped samples show a slight increase of their V_{cell} values as a consequence of the increase in the *c* parameter in comparison to the undoped TiO_2 sample, $Ti_{0.99}Ru_{0.01}O_2$ being the sample with the highest *c* and V_{cell} values. The increase of these parameters is most probably related to the increasing ionic radius of Re^{3+} ($r = 0.63$ Å) or Ru^{3+} ($r = 0.68$ Å) when replacing Ti^{4+} ($r = 0.605$ Å) [61] in the TiO_6 octahedra building blocks of the TiO_2 matrix, as well as the increase in the number of O vacancies induced by doping due to the unbalanced electrical charge and consequent cation repulsion. The clear change in the parameter *c* in comparison to *a* suggests that the dopant metal ions substitute Ti^{4+} preferentially at body centered and face centered lattice sites in the anatase matrix [42, 62].

The samples' mean crystallite sizes, <*D*>, were evaluated by Scherrer's equation [63] using the (101) plane reflections. The undoped $TiO_{2-\delta}$ sample shows a <*D*> value of 13.2 nm, while samples $Ti_{0.99}Re_{0.01}O_2$ and $Ti_{0.99}Ru_{0.01}O_2$ have mean crystallite sizes of 10.2 nm and 7.2 nm, respectively. The decrease in <*D*> inferred for the doped samples may be attributed to lattice distortions induced by the Re and Ru doping or to the possible formation of TM–O–Ti bonds that may prevent grain growth, in a similar manner to that observed for Mo-doped TiO_2 [42].

The morphology and structure of the nanoparticle samples were further investigated by transmission electron microscopy. Figure 2 shows three representative

Table 1 Lattice parameters, unit cell volumes, crystallite sizes, optical bandgap energies and Urbach energies of the different synthesized nanoparticles

Sample	Lattice parameters			Crystallite size (nm)		S_{BET} ($m^2\ g^{-1}$)	E_g (eV)	E_U (meV)
	a (Å)	*c* (Å)	V_{cell} ($Å^3$)	Scherrer[a]	TEM[b]			
Undoped TiO_2	3.786	9.396	134.673	13.2	14.3	78.3	3.26 ± 0.09	97.8 ± 0.8
$Ti_{0.99}Re_{0.01}O_2$	3.787	9.412	135.011	10.2	10.6	119.3	3.21 ± 0.11	301.4 ± 6.3
$Ti_{0.99}Ru_{0.01}O_2$	3.787	9.529	136.313	7.2	7.7	159.7	3.34 ± 0.09	329.1 ± 20.5

[a]Values calculated from XRD data using the Scherrer equation

[b]Values calculated from TEM image analyses

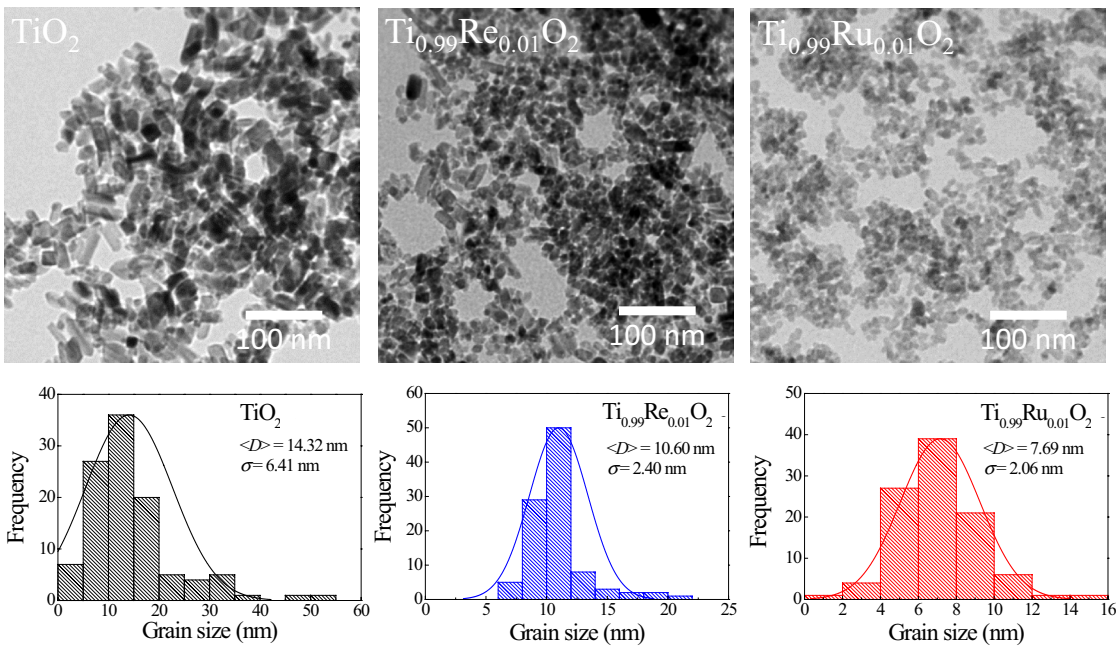

Fig. 2 TEM micrographs of undoped TiO_2, Re-doped TiO_2 and Ru-doped TiO_2 nanoparticle samples, and the corresponding particle size distribution histograms

bright field TEM micrographs of the different synthesised samples, as well as the respective particle size histograms. As can be seen, the undoped TiO_2 sample is composed of single crystalline nanoparticles of square or elongated shape with an irregular surface microstructure while those of doped samples present a much more uniform surface microstructure. The samples' particle size follows a lognormal distribution with mean sizes in good agreement with the size of the coherent diffracting domains calculated from the XRD pattern using Scherrer's equation.

The samples' specific surface area, S_{BET}, was evaluated by the B.E.T. method, the S_{BET} values thus determined being shown in Table 1. For pristine TiO_2 sample this is 78.3 $m^2\ g^{-1}$. As expected, the TM-doped samples have higher S_{BET} values in comparison to that of the undoped sample due to their smaller crystallite size. $Ti_{0.99}Re_{0.01}O_2$ and $Ti_{0.99}Ru_{0.01}O_2$ samples exhibit specific surface areas of 119.3 $m^2\ g^{-1}$ and 159.7 $m^2\ g^{-1}$. The importance of crystallite size for the photocatalytic activity of *anatase* TiO_2 has been clearly demonstrated [64, 65], its photocatalytic activity increasing with decreasing crystallite size. Moreover, it has been reported that the introduction of metal ions in the *anatase* TiO_2 matrix may lead to an increase of S_{BET} and to a decrease of the pore size via a filling effect [49, 66], thus favoring also the TiO_2 photocatalytic activity.

3.2 Optical spectroscopy

Optical characterization of the samples was done by measuring their diffuse reflectance, R, in the UV–Vis-IR region. R is related to the absorption Kubelka–Munk function, F_{KM}, by the relation $F_{KM}(R) = (1-R)^2/2R$, which is proportional to the absorption coefficient [67]. The samples' absorption spectra are shown in Fig. 3. As can be seen, all samples exhibit high absorption in the UV region and a strong decay as the visible region is approached. Nevertheless, it should be noted that TM-doped samples show absorption in all the visible region. On the other hand no significant shifts in the optical absorption band edge can be seen for the TM-doped samples compared to the undoped TiO_2. The indirect optical bandgap energies, E_g, of the different samples were calculated by plotting $f_{KM} = (F_{KM}h\nu)^{1/2}$ as a function of $h\nu$, where h is the Planck's constant and ν the radiation frequency, and by extrapolating the linear part of the curve to zero absorption [9], as shown in the upper panel plots of Fig. 4. The obtained E_g values are given in Table 1. The optical bandgap energy of the undoped TiO_2 sample was estimated as 3.26 ± 0.09 eV close to the TiO_2 *anatase* bulk reference value (3.2 eV). The $Ti_{0.99}Re_{0.01}O_2$ and $Ti_{0.99}Ru_{0.01}O_2$ samples exhibit E_g values of 3.21 ± 0.11 eV and 3.34 ± 0.09 eV, respectively. The slight blue shift observed for the Ru-doped TiO_2 bandgap is probably due to the Burstein–Moss (MB) effect [68, 69], since the average

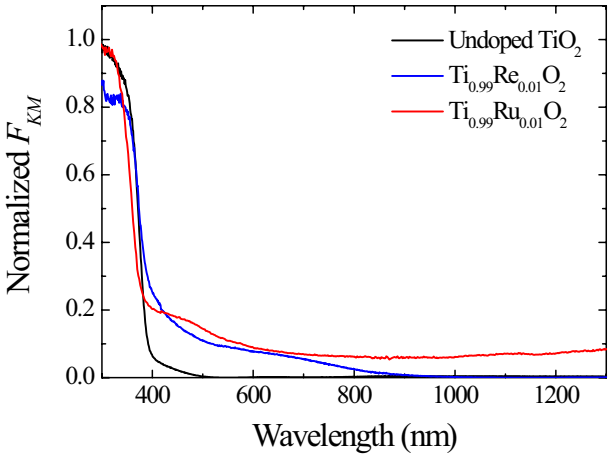

Fig. 3 Normalized absorption spectra of the different prepared nanoparticle samples

crystallite size of this sample (7.2 nm) is not in the range of the Bohr radius of the first excitonic state of the anatase TiO_2 ($r_B = 0.86$ nm) [59], and thus the quantum confinement effects associated with the nanosized crystallites are certainly very weak. Accordingly to the MB model, above the Mott critical density the partial filling of the conduction band leads to a blocking of the lowest states and thus to a widening of the bandgap.

Although the TM-doped samples show optical bandgap energies similar to the E_g value estimated for the undoped TiO_2 sample, their Urbach energies, E_U, are substantially higher as will be shown below. The Urbach energy is associated with the width of the Urbach tail, which follows the exponential law $\alpha = \alpha_0 \exp(h\nu/E_U)$, where α is the optical absorption coefficient and α_0 is a constant [70]. E_U is often interpreted as the width of the tail of localized states in the bandgap [71]. Since the absorption Kubelka–Munk function F_{KM} is proportional to the sample's absorption [67], the Urbach energies of the different synthesized nanoparticles were estimated from the slopes of $\ln(F_{KM})$ plotted as a function of the photon energy, in an energy range just below the bandgap, as shown in the lower panel plots of Fig. 4. The calculated E_U values are given in Table 1. As can be seen, while the undoped TiO_2 sample has an E_U value of 97.8 ± 0.8 meV, samples $Ti_{0.99}Re_{0.01}O_2$ and $Ti_{0.99}Ru_{0.01}O_2$ present E_U values of 301.8 ± 6.3 meV and 329.1 ± 20.5 meV, respectively. These remarkable E_U differences between the undoped sample and the TM-doped samples are related to the higher density of localized states in the bandgap, which might be associated with structural disorder/smaller crystallite sizes of both Re- and Ru-doped samples [71, 72] and/or with their crystal structural features inducing different crystal field strength splitting of the localized transition metal 3*d*-states along with oxygen defect band states, in a similar manner to that observed for *e.g.* Fe-doped TiO_2

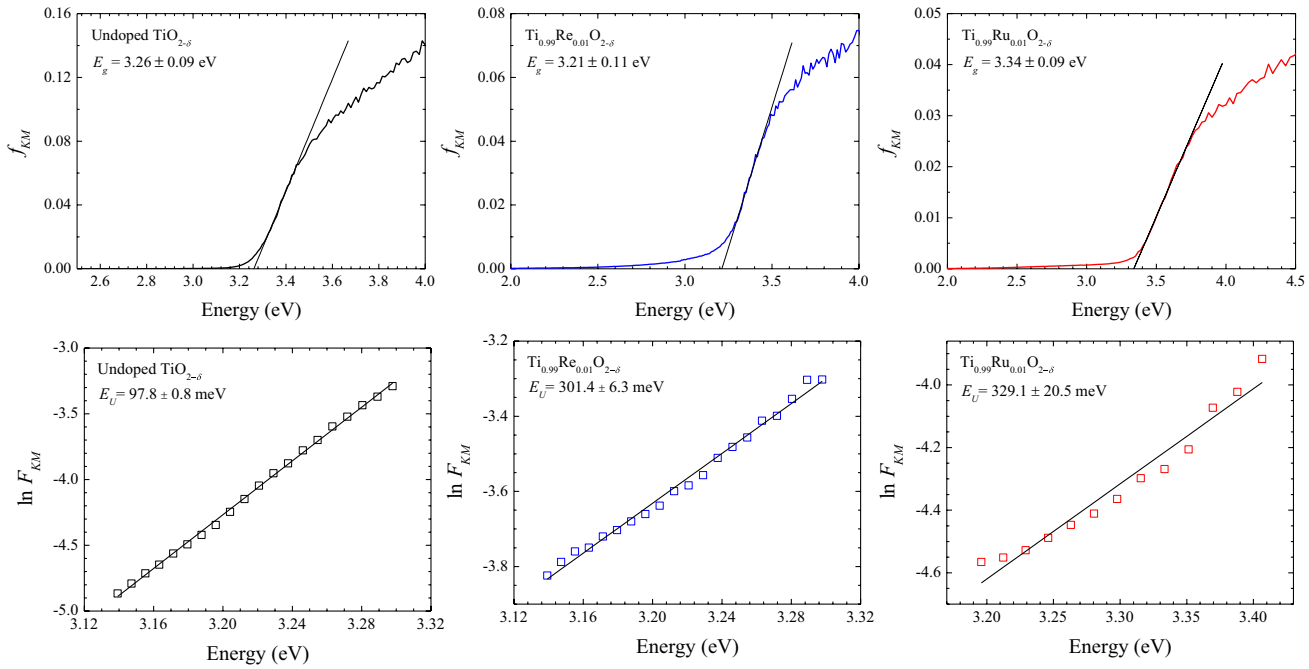

Fig. 4 Tauc plots of the undoped TiO_2 or TM-doped TiO_2 nanoparticle samples (upper panel plots) and ln F_{KM} versus photon energy plots allowing the evaluation of the Urbach energy of the different samples (lower panel plots)

nanoparticles [73], Co-doped SnO_2 [9] nanoparticles and Co-doped TiO_2 films [59, 60]. Nevertheless, the increase in the number of localized states in the bandgap may lead to a broadening of the absorption band tail and even to a decrease of the recombination rate of photocharge carriers via electron trapping phenomena [74] and thus to an increase of the materials' photocatalytic activity as intended.

3.3 Photoluminescence spectroscopy

To evaluate a possible photo-generated charge-carriers' recombination reduction due to metal doping, the photoluminescence (PL) of the different synthesized nanopowders was analyzed. The samples' PL spectra are shown in Fig. 5. In TiO_2 nanoparticles, the emission peak at ~ 400 nm is attributed to the bandgap transitions [75]. As can be seen from the obtained PL spectra, the Re- and Ru-doped TiO_2 samples show a clear intensity decrease of this peak. This result indicates a more efficient inhibition of the recombination of the photo-generated charge carriers of the doped semiconductor samples. The recombination reduction is more effective for the Ru-doped TiO_2 sample and may anticipate a better photocatalytic performance for this sample. This effect should be due to a more efficient electron–hole separation resulting from the creation of new energetic levels in the forbidden zone.

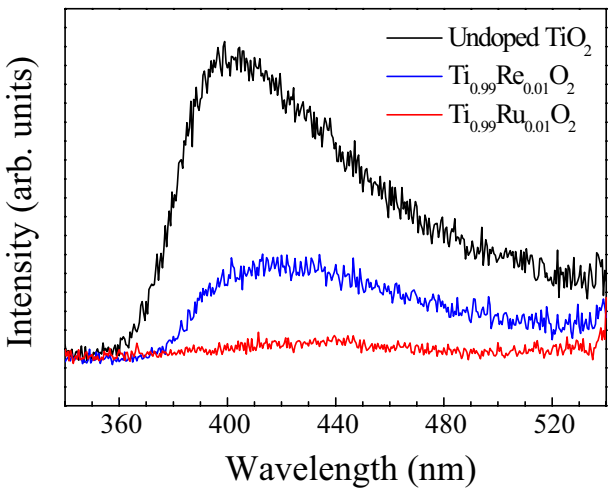

Fig. 5 Photoluminescence spectra of the different synthesized samples

3.4 Pollutants photocatalytic degradation

The potential photocatalytic ability of the different synthesized samples for the degradation of organic pollutants was studied by monitoring the photodegradation of two organic compounds in the presence of the different prepared samples. To evaluate their photocatalytic flexibility, a cationic compound (rhodamine B) and an anionic compound (phenol) were chosen as model pollutants.

3.4.1 RhB photodegradation

The photocatalytic efficiency of the undoped and TM-doped TiO_2 samples on the degradation of 10 ppm RhB solution was evaluated for 75 min of irradiation, after 60 min in dark. For comparative purposes the dye photolysis was also evaluated. The plots of Fig. 6 show the RhB absorption spectra during irradiation in the presence of the different prepared samples. The RhB typical absorption spectrum is characterized by one broad absorption band centred at 554 nm [76], which was used as a reference for the RhB photodegradation analysis. The dye adsorption is confirmed by the intensity decrease of the peak at $t = 0$ compared to the initial intensity. As can be seen, during irradiation the intensity of the characteristic dye absorption band gradually decreases with time, which indicates a progressive degradation of the organic compound. Taking into account the variation of the 554 nm absorption peak intensity, the RhB photodegradation profiles were plotted for all the samples tested and shown in Fig. 7. The photolysis profile is also shown as a reference. After 60 min in the dark, about 33%, 30% and 27% of the initial dye were removed from solution by adsorption, using $Ti_{0.99}Ru_{0.01}O_2$, $Ti_{0.99}Re_{0.01}O_2$ and undoped TiO_2 nanoparticles, respectively. After turning on the lamp, all samples demonstrated catalytic activity for the RhB photodegradation reaction, the more efficient photocatalyst being the Ru-doped TiO_2 sample. Indeed, a decrease of about 92% of the initial dye concentration was achieved after only 20 min of irradiation using $Ti_{0.99}Ru_{0.01}O_2$ nanoparticles as catalyst, the RhB being almost completely decomposed to colourless end products after 30 min of illumination. In comparison, decreases of about 97% and 92% of the initial RhB concentration were achieved for $Ti_{0.99}Re_{0.01}O_2$ and undoped $TiO_{2-\delta}$ samples, respectively, after 30 min of irradiation.

3.4.2 Phenol photodegradation

The photocatalytic efficiency of the undoped and TM-doped TiO_2 nanoparticle samples for the degradation of a 20 ppm phenol solution was studied for 75 min. Figure 8 shows the degradation profiles of the phenol solution in the presence of each prepared sample as well as the photolysis profile. First of all, it should be noted that the phenol adsorption by the different nanopowder samples is much lower than that observed for RhB. Indeed, after 60 min in dark ($t = 0$), only Re-doped TiO_2 was able to remove 11% of the initial phenol from solution by adsorption. Secondly, as for RhB degradation, all synthesized samples are catalytic for the phenol photodegradation reaction. Best results were also obtained for $Ti_{0.99}Ru_{0.01}O_2$ nanoparticles. After 45 min of irradiation, the phenol degradation was practically complete (98%) using this sample as a photocatalyst, while for the same irradiation period $Ti_{0.99}Re_{0.01}O_2$ and undoped TiO_2 samples achieved only 93% and 92% of phenol degradation, respectively.

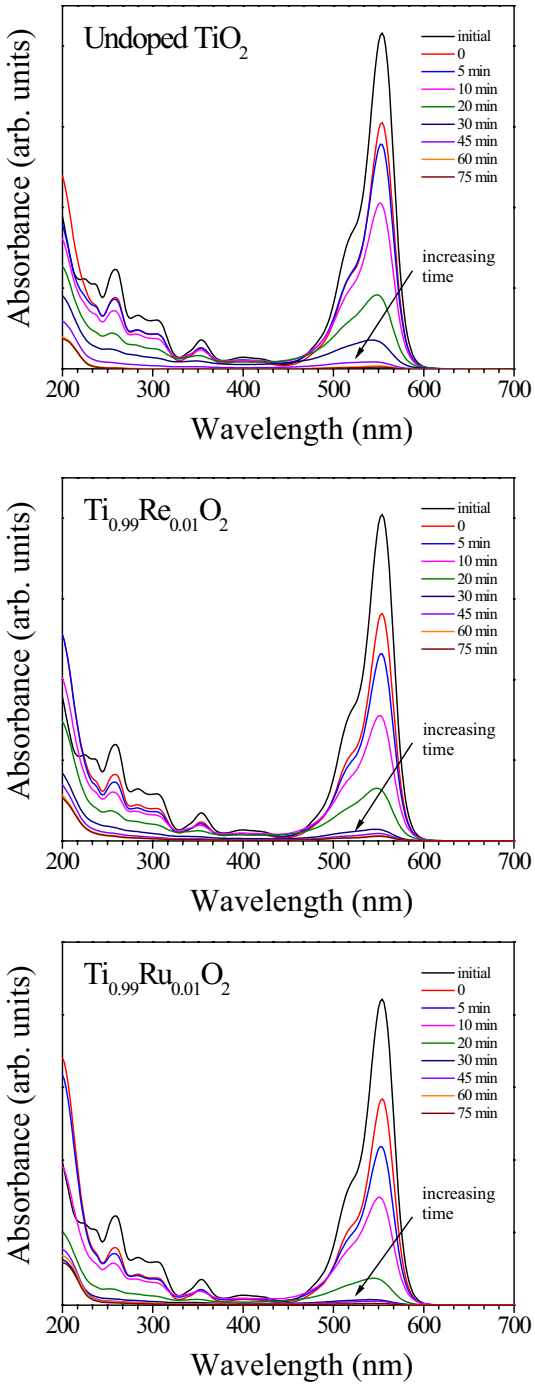

Fig. 6 Absorption spectra of a 10 ppm RhB solution using undoped TiO_2, Re-doped TiO_2 and Ru-doped TiO_2 samples as photocatalyst, up to 75 min of irradiation

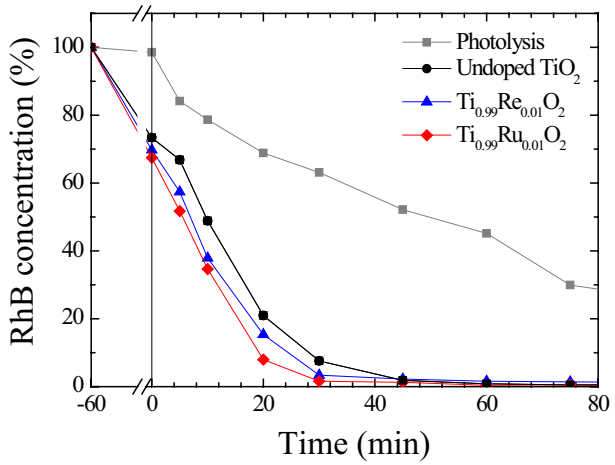

Fig. 7 Concentration of RhB versus irradiation time using the different prepared samples as photocatalysts

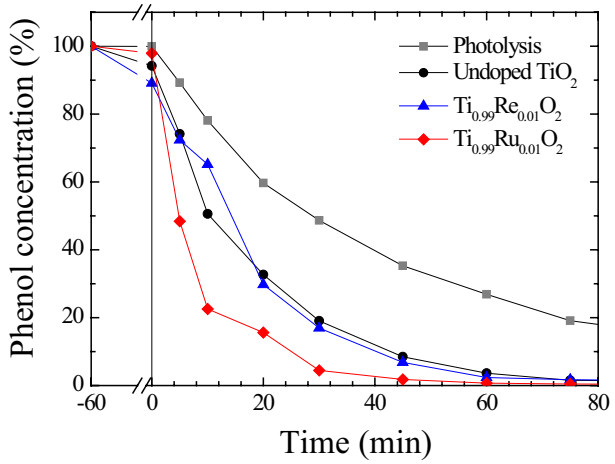

Fig. 8 Concentration of phenol versus irradiation time using the different prepared samples as photocatalysts

3.4.3 Kinetics studies

The RhB and phenol photodegradation profiles previously discussed allow us to go further into the kinetics of the several photo-oxidation reactions studied and compare quantitatively the photocatalytic efficiency of the different synthesized nanoparticle samples. At low concentrations, the photocatalytic degradation rate of most organic pollutants follows the pseudo-first order kinetics model [73, 77, 78] described by the rate equation $dC/dt = -k_{ap}C$, whose integration leads to the relation $C = C_0 \exp(-k_{ap}t)$, where C_0 stands for the pollutant concentration at $t = 0$, C is the pollutant concentration at time t, and k_{ap} is the apparent reaction rate constant. The half-life, $t_{1/2}$, of the organic pollutants can thus be calculated as $t_{1/2} = \ln 2/k_{ap}$.

Figure 9 shows the $\ln (C_0/C)$ versus t plots for the degradation reactions of 10 ppm RhB solution using the different prepared nanomaterial samples as photocatalysts for 30 min of irradiation. The respective k_{ap} and $t_{1/2}$ parameters are given in Table 2. As can be seen, good linear fits having *R-squared* great than 0.99 were obtained, which show that the RhB photodegradation reactions are described by the pseudo-first order kinetics model. The apparent first-order rate constants were deduced from the slope of the fitted straight line, with estimated k_{ap} values of $8.28 \times 10^{-2} \pm 2.68 \times 10^{-3}$ min^{-1}, $1.07 \times 10^{-1} \pm 5.20 \times 10^{-3}$ min^{-1} and $1.32 \times 10^{-1} \pm 5.07 \times 10^{-3}$ min^{-1} for the reactions using undoped TiO_2, $Ti_{0.99}Re_{0.01}O_2$ and $Ti_{0.99}Ru_{0.01}O_2$ nanoparticles as photocatalysts, respectively. Therefore, for the experimental conditions used, the photocatalytic efficiency of Ru-doped TiO_2 for the RhB photo-oxidation reaction is ~ 37% higher than the TiO_2 photocatalytic efficiency.

Similar results were obtained for the phenol photodegradation. Figure 10 shows the reaction kinetics of 20 ppm phenol solution for 45 min using the different prepared nanoparticle samples as photocatalysts. The deduced kinetics parameters are shown in Table 2. As for the RhB, also the phenol photodegradation reactions follow pseudo-first order kinetics. An apparent reaction rate constant of $9.58 \times 10^{-2} \pm 5.89 \times 10^{-3}$ min^{-1} was obtained when using $Ti_{0.99}Ru_{0.01}O_2$ nanoparticles as photocatalyst, while k_{ap} values of $5.92 \times 10^{-2} \pm 1.44 \times 10^{-3}$ min^{-1} and $5.55 \times 10^{-2} \pm 1.13 \times 10^{-3}$ min^{-1} were deduced for the reactions in the presence of $Ti_{0.99}Re_{0.01}O_2$ and undoped TiO_2 nanoparticles, respectively. Thus, the Ru-doped TiO_2 sample shows photocatalytic efficiency for the phenol photodegradation reaction about 42% higher than that of undoped TiO_2.

Overall, these results confirm that doping either with Re or Ru can lead to an enhancement of the TiO_2 photocatalytic efficiency and that Ru-doped TiO_2 are the most efficient photocatalyst for both the RhB and phenol photodegradation reactions, among the synthesized TiO_2 based nanopowder samples. Comparison with other TiO_2-based photocatalysts should be made with caution because not only is the literature extensive, but the conditions under which the photodegradation assays are carried out are quite different in both photocatalyst/organic compound concentrations and irradiation conditions. Nevertheless, our results shows that all the synthesized samples offer better photocatalytic performance for the studied reactions than the commercial Degussa P25 TiO_2 [79, 80], nanostructured TiO_2 [81] and TiO_2 modified by post-treatment with phosphorous acid [79]. In particular, Ru-doped TiO_2 seems to be a very promising photocatalyst, with a photocatalytic performance being seemingly better than other TiO_2-based materials such as Fe-doped TiO_2 [80] and C–N–S tridoped TiO_2 [82] or even than the more complex

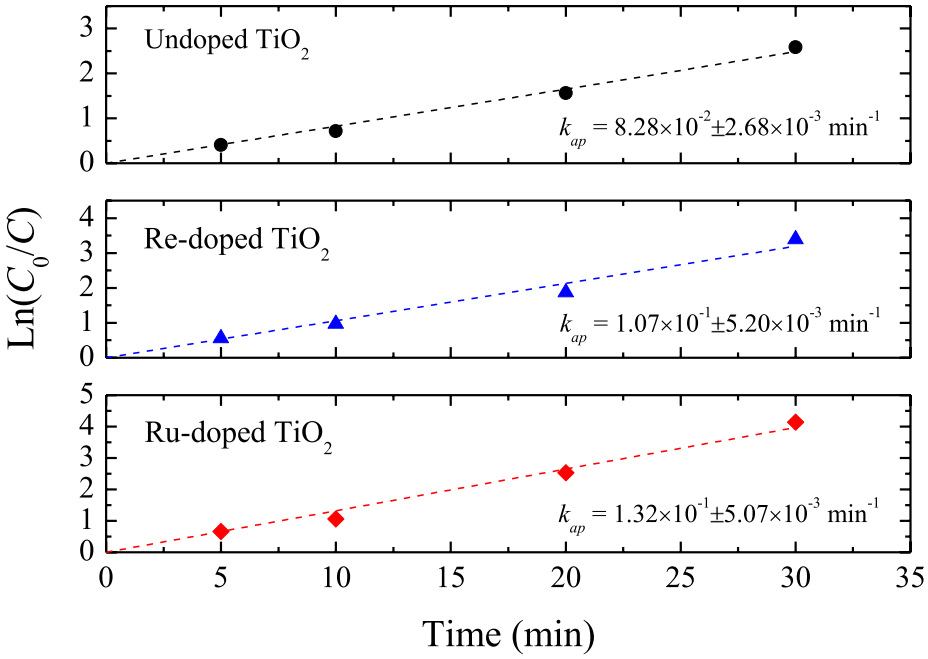

Fig. 9 Kinetics of the RhB photodegradation reactions using undoped TiO_2, Re-doped TiO_2 and Ru-doped TiO_2 samples as photocatalyst

Table 2 Apparent first-order rate constants and half-life values of both RhB and phenol photodegradation reactions using the different synthesized nanoparticles as photocatalysts

Sample	RhB photodegradation			Phenol photodegradation		
	k_{ap} (min^{-1})	$t_{1/2}$ (min)	R^2	k_{ap} (min^{-1})	$t_{1/2}$ (min)	R^2
Undoped TiO_2	$8.28\times10^{-2}\pm2.68\times10^{-3}$	8.02 ± 0.20	0.997	$5.55\times10^{-2}\pm1.13\times10^{-3}$	12.54 ± 0.16	0.999
$Ti_{0.99}Re_{0.01}O_2$	$1.07\times10^{-1}\pm5.20\times10^{-3}$	7.39 ± 0.48	0.993	$5.92\times10^{-2}\pm1.44\times10^{-3}$	11.39 ± 0.22	0.997
$Ti_{0.99}Ru_{0.01}O_2$	$1.32\times10^{-1}\pm5.07\times10^{-3}$	6.20 ± 0.50	0.991	$9.58\times10^{-2}\pm5.89\times10^{-3}$	7.79 ± 0.42	0.993

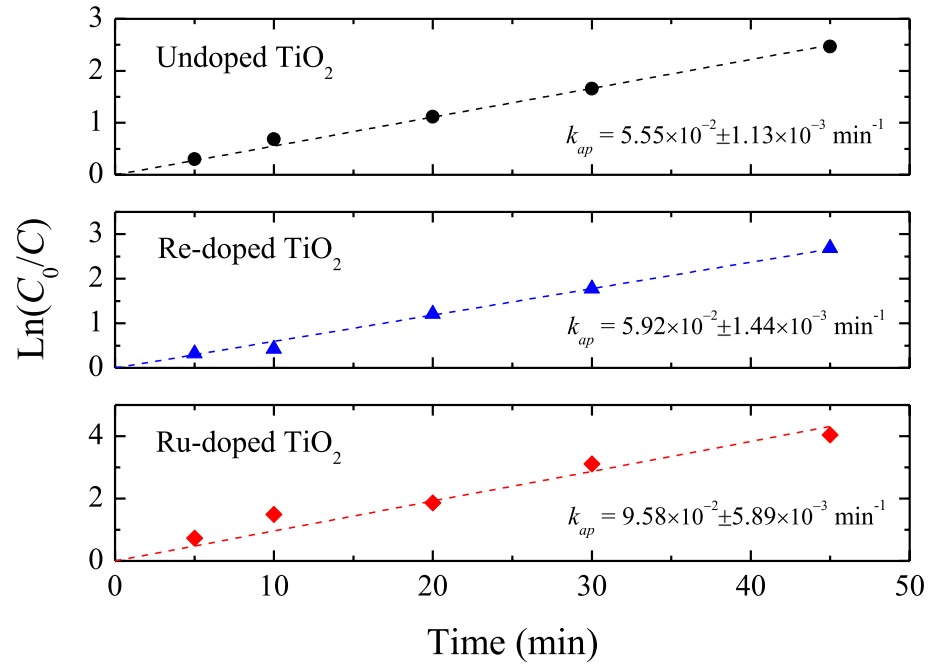

Fig. 10 Kinetics of the phenol photodegradation reactions using undoped TiO_2, Re-doped TiO_2 and Ru-doped TiO_2 samples as photocatalyst

TiO_2/C-dot [83] and porous TiO_2-SnO_2 nanocomposites [84].

4 Conclusions

TiO_2, Re-doped TiO_2 and Ru-doped TiO_2 anatase nanopowders samples with a nominal TM/Ti ratio of 0.01 were successfully synthesized via a simple hydrothermal method, which is cost effective. The lattice parameters of the different prepared samples were calculated and their mean crystallite sizes determined to be in the range 15–7 nm, the lower <*D*> values being obtained for the TM-doped samples probably due to lattice distortions induced by Re and Ru doping and/or to the possible formation of TM–O–Ti bonds that may prevent grain growth. The incorporation of the dopant elements results in an increase of the optical absorption in the visible range. The optical bandgap and Urbach energies of the samples were calculated. Although the TM-doped samples show optical bandgap energies similar to that estimated for the TiO_2 sample (3.26 ± 0.09 eV), their Urbach energies are significant higher. E_U values of 97.8 ± 0.8 meV, 301.8 ± 6.3 meV and 329.1 ± 20.5 meV were obtained for the undoped TiO_2, Re-doped TiO_2 and Ru-doped TiO_2 samples, respectively. The higher E_U values deduced for the doped samples might be related to the higher density of localized states in the bandgap associated with structural disorder/smaller crystallite sizes of both Re- and Ru-doped samples and with localized transition metal 3*d*-states in the bandgap along with oxygen defect band states induced charge compensation.

The photocatalytic behavior of the synthesized samples was investigated for the RhB and phenol degradation processes under UV–Vis irradiation, the kinetics of the different photo-oxidation reactions was also studied and the apparent first-order rate constants and half-lifes determined. Results showed that doping either with Re or Ru can lead to an enhancement of the TiO_2 photocatalytic efficiency and that Ru-doped TiO_2 are, among the synthesized samples, the most efficient photocatalyst for both the RhB and phenol photodegradation reactions. The high photocatalytic efficiency observed for the Ru-doped TiO_2 sample is probably connected with its higher S_{BET} value, which allows more organic molecules to attach to the active sites of the photocatalytic nanoparticles, and to the increase in the number of localized states in the bandgap that may induce a broadening of the absorption band tail and electron trapping phenomena.

Acknowledgements This work has been partially supported by the Portuguese Foundation for Science and Technology (FCT) under the UID/CTM/04540/2013 UID/MULTI/00612/2019 and IF/01210/2014. B. Barrocas acknowledge FCT for her Ph.D. Grant (SFRH/BD/101220/2014). The authors thank P.I.C. Teixeira for critically reading of the manuscript.

Compliance with ethical standards

Conflict of interest The authors declare that they have no conflict of interest.

References

1. Deng Y, Zhao R (2015) Advanced oxidation processes (AOPs) in wastewater treatment. Curr Pollut Rep 1:167–176
2. Ameta R, Kumar A, Punjabi PB, Ameta CS (2013) Advanced oxidation processes: basics and applications. In: Rai DG, Senthikumar R, Byrne JA, Feroz S (eds) Wastewater treatment: advanced processes and technologies. CRC Press, London
3. Bethi B, Sonawane SH, Bhanvase BA, Gumfekar SP (2016) Nanomaterials-based advanced oxidation processes for wastewater treatment: a review. Chem Eng Proc 109:178–189
4. Hoffmann MR, Martin ST, Choi W, Bahnemann DW (1995) Environmental applications of semiconductor photocatalysis. Chem Rev 95:69–96
5. Litter MI (1999) Heterogeneous photocatalysis transition metal ions in photocatalytic systems. Appl Catal B 23:89–114
6. Ayoub K, van Hullebusch ED, Cassir M, Bermond A (2010) Application of advanced oxidation processes for TNT removal: a review. J Hazard Mater 178:10–28
7. Lü J, Lin J-X, Zhao X-L, Cao R (2012) Photochromic hybrid materials of cucurbituril and polyoxometalates as photocatalysts under visible ligh. Chem Commun 48:669–671
8. Du JJ, Yuan YP, Sun JX, Peng FM, Jiang X, Qiu LG, Xie AJ, Shen YH, Zhu JF (2011) New photocatalysts based on MIL-53 metal–organic frameworks for the decolorization of methylene blue dye. J Hazard Mater 190:945–951
9. Entradas T, Cabrita J, Dalui S, Nunes MR, Monteiro OC, Silvestre AJ (2014) Synthesis of sub-5 nm Co-doped SnO_2 nanoparticles and their structural, microstructural, optical and photocatalytic properties. Mater Chem Phys 147:563–571
10. Barrocas B, Silvestre AJ, Rolo AR, Monteiro OC (2016) The effect of ionic Co presence on the structural, optical and photocatalytic properties of modified cobalt-titanate nanotubes. Phys Chem Chem Phys 18:18081–18093
11. Entradas TJ, Cabrita JC, Barrocas B, Nunes MR, Silvestre AJ, Monteiro OC (2015) Synthesis of titanate nanofibers co-sensitized with ZnS and Bi_2S_3 nanocrystallites and their application on pollutants removal. Mater Res Bull 72:20–28
12. Ferreira VC, Nunes MR, Silvestre AJ, Monteiro OC (2013) Synthesis and properties of Co-doped titanate nanotubes and their optical sensitization with methylene blue. Mater Chem Phys 142:355–362
13. Bem V, Neves MC, Nunes MR, Silvestre AJ, Monteiro OC (2012) Influence of the sodium content in the structural, morphological and photocatalytic properties of titanate nanotubes. J Photochem Photobiol A 232:50–56
14. Prakash J, Sun S, Swart HC, Gupta RK (2018) Noble metals-TiO_2 nanocomposits: from fundamental mechanisms to photocatalysis, surface enhanced Raman scattering and antibacterial applications. Appl Mater Today 11:82–135
15. Yang Y, Flatebo C, Liang J, Dong P, Yuan J, Wang T, Zhang J, Chen W, Wu J, Ajayan PM, Ci L, Li Q, Lou J (2016) Towards methyl orange degradation by direct sunlight using coupled

TiO_2 nanoparticles and carbonized cotton T-shirt. Appl Mater Today 3:57–62
16. Nakata K, Fujishima A (2012) TiO_2 photocatalysis: design and applications. J Photochem Photobiol C 13:169–189
17. Thiruvenkatachari R, Vigneswaran S, Moon IS (2008) Review on UV/TiO_2 photocatalytic oxidation process. Korean J Chem Eng 25:64–72
18. Lazar MA, Varghese S, Nair SS (2012) Photocatalytic water treatment by titanium dioxide: recent updates. Catalysts 2:572–601
19. Bellardita M, Di Paola A, Megna B, Palmisano L (2018) Determination of the crystallinity of TiO_2 photocatalysts. J Photochem Photobiol A 367:312–320
20. Silva EP, Winkler MEG, Giufrida WM, Cardozo-Filho L, Alonso C-G, Lopes JBO, Rubira AF, Silva R (2019) Effect of phase composition on the photocatalytic activity of titanium dioxide obtained from supercritical antisolvent. J Colloid Interface Sci 535:245–254
21. The international Centre for Diffraction Data®, JCPDS Database Card No. 21-1276
22. The international Centre for Diffraction Data®, JCPDS Database Card No. 21-1272
23. Pillai SC, Periyat P, George R, McCormack DE, Seery MK, Hayden H, Colreavy J, Corr D, Hinder SJ (2007) Synthesis of high-temperature stable anatase TiO_2 photocatalyst. J Phys Chem C 111:1605–1611
24. Castro AL, Nunes MR, Carvalho AP, Costa FM, Florêncio MH (2008) Synthesis of anatase TiO_2 nanoparticles with high temperature stability and photocatalytic activity. Sol Stat Sci 10:602–611
25. Larumbe S, Monge M, Gómez-Polo C (2015) Comparative study of (N, Fe) doped TiO_2 photocatalysts. Appl Surf Sci 327:490–497
26. Liu L, Zhao H, Andino JM, Li Y (2012) Photocatalytic CO_2 reduction with H_2O on TiO_2 nanocrystals: comparison of anatase, rutile, and brookite polymorphs and exploration of surface chemistry. ACS Catal 2:1817–1828
27. Lu T, Wang Y, Wang Y, Zhou L, Yang X, Su Y (2017) Synthesis of mesoporous anatase TiO_2 sphere with high surface area and enhanced photocatalytic activity. J Mater Sci Technol 33:300–304
28. Medana C, Calza P, Dal Bello F, Raso E, Minero C, Baiocchi C (2011) Multiple unknown degradants generated from the insect repellent deet by photoinduced processes on TiO_2. J Mass Spectrom 46:24–40
29. Lopez-Alvarez B, Torres-Palma RA, Penuela G (2011) Solar photocatalitycal treatment of carbofuran at lab and pilot scale: effect of classical parameters, evaluation of the toxicity and analysis of organic by-products. J Hazard Mater 191:196–203
30. Stapleton DR, Konstantinou IK, Mantzavinos D, Hela D, Papadaki M (2010) On the kinetics and mechanisms of photolytic/TiO_2-photocatalytic degradation of substituted pyridines in aqueous solutions. Appl Catal B 95:100–109
31. An TC, An JB, Yang H, Li GY, Feng HX, Nie XP (2011) Photocatalytic degradation kinetics and mechanism of antivirus druglamivudine in TiO_2 dispersion. J Hazard Mater 197:229–236
32. Lu C-S, Chen C-C, Mai F-D, Li H-K (2009) Identification of the degradation pathways of alkanolamines with TiO_2 photocatalysis. J Hazard Mater 165:306–316
33. Asahi R, Morikawa T, Ohwaki T, Aoki K, Taga Y (2001) Visible-light photocatalysis in nitrogen-doped titanium oxides. Science 293:269–271
34. Li C, Yang W, Li Q (2018) TiO_2-based photocatalysts prepared by oxidation of TiN nanoparticlesand their photocatalytic activities under visible light illumination. J Mater Sci Technol 34:969–975
35. Cheng C, Sun Y (2012) Carbon doped TiO_2 nanowire arrays with improved photoelectrochemical water splitting performance. Appl Surf Sci 263:273–276
36. Ohnoa T, Akiyoshi M, Umebayashi T, Asai K, Mitsui T, Matsumura M (2004) Preparation of S-doped TiO_2 photocatalysts and their photocatalytic activities under visible light. Appl Catal A 265:115–121
37. Ali T, Tripathi P, Azam A, Raza W, Ahmed AS, Ahmed A, Muneer M (2017) Photocatalytic performance of Fe-doped TiO_2 nanoparticles under visible-light irradiation. Mater Res Express 4:015022
38. Wang T, Meng X, Liu G, Chang K, Li P, Kang Q, Liu L, Li M, Ouyang S, Ye J (2015) In situ synthesis of ordered mesoporous Co-doped TiO_2 and its enhanced photocatalytic activity and selectivity for the reduction of CO_2. J Mater Chem A 3:9491–9501
39. Peng Y-H, Huang G-F, Huang W-Q (2012) Visible-light absorption and photocatalytic activity of Cr-doped TiO_2 nanocrystal films. Adv Powder Technol 23:8–12
40. Yang X-J, Wang S, Sun H-M, Wang X-B, Lian J-S (2015) Preparation and photocatalytic performance of Cu-doped TiO_2 nanoparticles. Trans Nonferrous Met Soc China 25:504–509
41. Wang RSH, Feng J, Hu X, Lock PY (2004) Discoloration and mineralization of non-biodegradable azo dye orange II by copper-doped TiO_2 nanocatalysts. J Environ Sci Health Part A Toxic/Hazard Subst Environ Eng 39:2583–2595
42. Devi LG, Kumar SG, Murthy BN, Kottam N (2009) Influence of Mn^{2+} and Mo^{6+} dopants on the phase transformations of TiO_2 lattice and its photocatalytic activity under solar illumination. Catal Commun 10:794–798
43. Singh N, Prakash J, Misra M, Sharma A, Gupta RK (2017) Dual functional Ta-doped electrospun nanofibers with enhanced photocalysis and SERS detection for organic compounds. ACS Appl Mater Interf 9:28495–28507
44. Yan N, Zhu Z, Zhang J, Zhao Z, Liu Q (2012) Preparation and properties of Ce-doped TiO_2 photocatalyst. Mater Res Bull 47:1869–1873
45. Choudhury B, Borah B, Choudhury A (2012) Extending photocatalytic activity of TiO_2 nanoparticles to visible region of illumination by doping of cerium. Photochem Photobiol 88:257–264
46. Quan X, Tan H, Zhao Q, Sang X (2007) Preparation of lanthanum-doped TiO_2 photocatalysts by coprecipitation. J Mater Sci 42:6287–6296
47. Huang Y, Cao J-J, Kang F, You S-J, Chang C-W, Wang Y-F (2017) High selectivity of visible-light-driven La-doped TiO_2 Photocatalysts for NO removal. Aerosol Air Qual Res 17:2555–2565
48. Meng F, Li J, Hong Z, Zhi M, Sakla A, Xiang C, Wu N (2013) Photocatalytic generation of hydrogen with visible-light nitrogen-doped lanthanum titanium oxides. Catal Today 199:48–52
49. Paul S, Chetri P, Choudhury B, Ahmed GA, Choudhury A (2015) Enhanced visible light photocatalytic activity of Gadolinium doped nanocrystalline titania: an experimental and theoretical study. J Colloid Interface Sci 439:54–61
50. Khade GV, Gavade NL, Suwarnkar MB, Dhanavade MJ, Sonawane KD, Garadkar KM (2017) Enhanced photocatalytic activity of europium doped TiO_2 under sunlight for the degradation of methyl orange. J Mater Sci Mater Electron 28:11002–11011
51. Xiong LB, Li JL, Yang B, Yu Y (2012) Ti^{3+} in the surface of titanium dioxide: generation, properties and photocatalytic application. J Nanomaterials 2012:1–13
52. Liu G, Yang HG, Wang X, Cheng L, Lu H, Wang L, Lu GQ, Cheng HM (2009) Enhanced photoactivity of oxygen deficient anatase TiO_2 with dominant 001 facets. J Phys Chem C 113:21784–21788
53. Misra M, Singh N, Gupta RK (2017) Enhanced visible-light-driven photocatalytic of Au@Ag core-shell bimetallic nanoparticles immobilized on electrospun TiO2 nanofibers for degradation of organic compounds. Catal Sci Technol 7:570–580
54. Singh N, Prakash J, Gupta RK (2017) Design and ngineering of high performance photocatalytic systems based on metal oxide-graphene-noble metal nanocomposites. Mol Syst Des Eng 2:422–439

55. Truppi A, Petronella F, Placido T, Striccoli M, Agostiano A, Curri ML, Comparelli R (2017) Visible-light-active TiO_2-based hybrid nanocatalysts for environmental applications. Catalysts 7:100
56. Singh N, Mondal K, Misra M, Sharma A, Gupta RK (2016) Quantum dot sensitized electrospun mesoporous titanium dioxide hollow nanofibers for photocatalytic applications. RSC Adv 6:48109–48119
57. Singh N, Chakraborty R, Gupta RK (2018) Mutton bone derived hydroxyapatite supported TiO_2 nanoparticles for sustainable photocatalytic applications. J Environ Chem Eng 6:459–467
58. Sahu M, Biswas P (2011) Single-step processing of copper-doped titania nanomaterials in a flame aerosol reactor. Nanoscale Res Lett 6:441
59. Rout S, Popovici N, Dalui S, Paramês ML, da Silva RC, Silvestre AJ, Conde O (2013) Phase growth control in low temperature PLD Co: TiO_2 films by pressure. Curr Appl Phys 13:670–676
60. Silvestre AJ, Rout S, Dalui S, Pereira LCJ, Viana AS, Conde O (2017) Co and (Co, Mo) doping effects on the properties of highly reduced TiO_2 anatase thin films. Curr Appl Phys 17:174–180
61. Shannon RD (1976) Revised effective ionic radii and systematic studies of interatomic distances in halides and chalcogenides. Acta Crystallogr A 32:751–767
62. Seebauer EG, Kratzer M (2009) Charged semiconductor defects: structure, thermodynamics and diffusion. Springer, London, p 269
63. Cullity BD, Stock SR (2001) Elements of X-ray diffraction, 3rd edn. Prentice Hall, New Jersey, p 99
64. Turchi C, Ollis DF (1990) Photocatalytic degradation of organic water contaminants: mechanisms involving hydroxyl radical attack. J Catal 122:178–192
65. Riviera AP, Tanaka K, Hinsanaga T (1997) Photocatalytic degradation of pollutant over TiO_2 in different crystal structures. Appl Catal B Environ 3:37–44
66. Chen D, Zhu Q, Lv Z, Deng X, Zhou F, Deng Y (2012) Microstructural and photocatalytic properties of Eu-doped mesoporous titanium dioxide nanoparticles by sol-gel method. Mater Res Bull 47:3129–3134
67. Kortüm G (1969) Reflectance Spectroscopy: Principles, Methods and Applications. Springer, New York, p 180
68. Hamberg I, Granqvist CG, Berggren K-F, Sernelius BE, Engström (1984) Band-gap widening in heavily Sn-doped In_2O_3. Phys Rev B 39:3240–3249
69. Choudhury B, Choudhury A (2013) Lattice distortion and corresponding changes in optical properties of CeO2 nanoparticles on Nd doping. Curr Appl Phys 143:217–223
70. Urbach F (1953) The long-wavelength edge of photographic sensitivity and of the electronic absorption of solids. Phys Rev 92:1324
71. Ikhmayies SJ, Ahmad-Bitar RN (2013) A study of the optical bandgap energy and Urbach tail of spray-deposited CdS: in thin films. J Mater Res Technol 2:221–227
72. Singh S, Li C, Panzer F, Narasimhan KL, Graeser A, Gujar TP, Köhler A, Thelakkat M, Huettner S, Kabra D (2016) Effect of thermal and structural disorder on the electronic structure of hybrid perovskite semiconductor $CH_3NH_3PbI_3$. J Phys Chem Lett 7:3014–3021
73. Khan H, Swati IK (2016) Fe^{3+}-doped anatase TiO_2 with d–d transition, oxygen vacancies and Ti^{3+} centers: synthesis, characterization, UV–vis photocatalytic and mechanistic studies. Ind Eng Chem Res 55:6619–6633
74. Ola O, Maroto-Valer MM (2015) Review of material design and reactor engineering on TiO_2 photocatalysis for CO_2 reduction. J Photochem Photobiol C 24:16–42
75. Mathew S, Prasad AK, Benoy T, Rakesh PP, Hari M, Libish TM, Radhakrishnan P, Nampoori VPN, Vallabhan CPG (2012) UV–visible photoluminescence of TiO_2 nanoparticles prepared by hydrothermal method. J Fluoresc 22:1563–1569
76. Kemnitz K, Tamai N, Yamazaki I, Yoshihara K (1986) Fluorescence decays and spectral properties of rhodamine B in submonomono- and multilayer systems. J Phys Chem 90:5094–5101
77. Asenjo NG, Santamaria R, Blanco C, Granda M, Álvarez P, Menéndez R (2013) Correct use of the Langmuir-Hinshelwood equation for proving the absence of a synergy effect in the photocatalytic degradation of phenol on a suspended mixture of titania and activated carbon. Carbon 55:62–69
78. Zhou M, Yu J, Cheng B (2006) Effects of Fe-doping on the photocatalytic activity of mesoporous TiO_2 powders prepared by an ultrasonic method. J Hazard Mater 137:1838–1847
79. Qin X, Jing L, Tian G, Qu Y, Feng Y (2009) Enhanced photocatalytic activity for degrading rhodamine B solution of commercial Degussa P25 TiO2 and its mechanism. J Hazard Mater 172:1168–1174
80. Borji SH, Nasseri S, Mahvi AH, Nabizadeh R, Javadi AH (2014) Investigation of photocatalytic degradation of phenol by Fe(III)-doped TiO_2 and TiO_2 nanoparticles. J Environ Health Sci Eng 12:101
81. Dodoo-Arhin D, Buabeng FP, Mwabora JM, Amaniampong PN, Agbe H, Nyankson E, Obada DO, Asiedu NY (2018) The effect of titanium dioxide synthesis technique and its photocatalytic degradation of organic dye pollutants. Heliyon 4:e00681
82. Amreetha S, Dhanuskodia S, Nithya A, Jothivenkatachalam K (2015) Photocatalytic degradation of rhodamine B by C–N–S tridoped TiO_2 nanoparticles. In: Teherani FH, Look DC, Roger DJ (eds) Proceedings of SPIE oxide-based materials and devices VI, vol 9364, p 93641Q
83. Ali SMYMM, Sandhya KY (2017) Novel approach for P25-carbon dot composite and the reactive oxygen species involved in the visible light photocatalytic mineralization of rhodamine B. ChemistrySelect 2:11840–11845
84. Wang Y, Yan Z, Wang X (2014) Photocatalytic degradation of rhodamine B dye over novel Porous TiO_2-SnO_2 nanocomposites prepared by hydrothermal method. Int J Photoenergy 2014:928519